Understanding the Lithium Storage Mechanism of $Ti_3C_2T_x$ MXene

Renfei Cheng,[†,‡] Tao Hu,[†,§,∥] Hui Zhang,[⊥] Chunmei Wang,[†,‡] Minmin Hu,[†,‡] Jinxing Yang,[†,‡] Cong Cui,[†,‡] Tianjia Guang,[†,‡] Changji Li,[†] Chao Shi,[†] Pengxiang Hou,[†] and Xiaohui Wang[*,†]

[†] Shenyang National Laboratory for Materials Science, Institute of Metal Research, Chinese Academy of Sciences, Shenyang 110016, China [‡] School of Materials Science and Engineering, University of Science and Technology of China, Shenyang 110016, China [§] University of Chinese Academy of Sciences, Beijing 100049, China [∥] Institute of Materials Science and Devices, Suzhou University of Science and Technology, Suzhou 215009, China [⊥]Department of Materials Science and Engineering, Monash University, Clayton, Victoria 3800, Australia

*E-mail: wang@imr.ac.cn.

Abstract

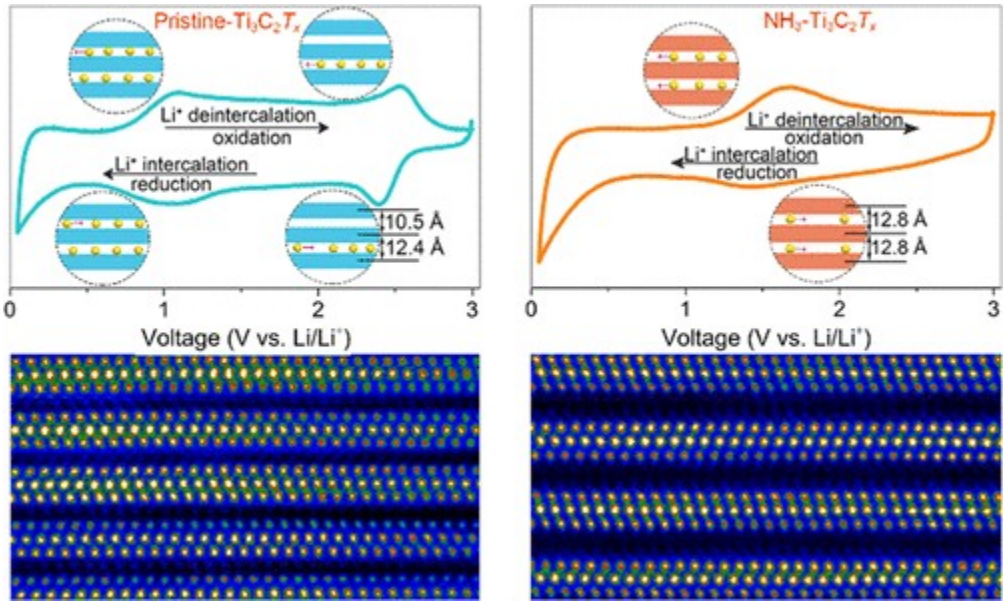

MXenes, as an emerging family of conductive two-dimensional materials, hold promise for late-model electrode materials in Li-ion batteries. A primary challenge hindering the development of MXenes as electrode materials is that a complete understanding of the intrinsic storage mechanism underlying the charge/discharge behavior remains elusive. This article presents two key discoveries: first, the characteristics of the $Ti_3C_2T_x$ structure can be modified systematically by calcination in various atmospheres, and second, these structural changes greatly affect Li-ion storage behavior, which reveals the mechanism for lithium storage in $Ti_3C_2T_x$ MXene. Specifically, via ammonization, the interlayer spacing gets dilated and uniform, giving rise to only one redox couple. In stark contrast, there are two well-recognized redox couples corresponding to two interlayer spacings in pristine $Ti_3C_2T_x$ MXene, in which Li-ion (de)intercalation occurs between interlayers in a sequential

manner as evidenced by ex situ X-ray diffraction (XRD). Notably, the XRD diffraction peaks shift hardly in the whole range of charge/discharge voltage, indicating a zero-strain feature upon Li-ion (de)intercalation. Moreover, the diffusion-controlled contribution percentage to capacity inversely depends on the scan rate. The understanding suggests a new design principle of the MXene anode: reduced lateral size to shorten the diffusion path and dilated interlayer spacing.

1. Introduction

The widespread applications of Li-ion batteries (LIBs) promote extensive studies on high-performance electrode materials.(1,2) As the common commercial anode material, graphite, suffers serious structure collapse during high-rate cycling since lithium intercalation in graphitic interlayers leads to dilation by up to 10.3%,(3,4) which cannot meet the requirement of high-rate LIBs in the future.(5) To address this critical issue, great efforts have been made to find alternative zero-strain anode materials to graphite.(6−8) Recently, MXenes,(9) as an emerging family of two-dimensional materials, have shown great promise for LIBs due to favorable electronic conductivity, good structural/chemical stability, inherently large interlayer spacing, and redox-active surface area and low diffusion barriers for Li ion mobility.(10−13)

So far, MXenes have been investigated as high-performance electrode materials in a variety of fields. These fields include, but not limited to LIBs,(14−16) sodium-ion batteries (SIBs),(17−19) Li–S batteries,(20−23) and supercapacitors.(24−26) In such investigations, MXenes were used as pristine, or by (i) surface modification, (ii) interlayer spacing modulation, and (iii) hybridizing with large-capacity pure metal or metal compounds. As far as surface modification is concerned, the surface chemistry of MXene was modified by heat treatment in various atmospheres, such as Ar, N_2, N_2/H_2, CO_2, and NH_3.(27−30) Many efforts have also been devoted to tuning interlayer spacing to modulate the electrochemical properties of MXene. As demonstrated, the interlayer spacings of MXenes can be readily tailored by creating pillared structures based on the spontaneous intercalation of surfactants.(31) Fortunately, MXenes with versatile chemical and structural variety provide excellent opportunities for constructing novel hybrid systems by incorporating various materials such as polymers,(32,33) carbon nanotubes,(18,34,35) and metal oxides/sulfides (e.g., TiO_2,(36) SnO_2,(15) Sb_2O_3,(37) MoS_2,(38) SnS_2,(39) and so forth), which exhibit greatly improved performance for supercapacitors, LIBs, and SIBs.

In spite of the intensive property explorations, the understanding of MXenes stops almost at theoretical predictions, leaving extremely limited experimental recognitions on their intrinsic storage mechanisms.(10,40,41) To the best knowledge of the authors, only V_2CT_x and $Ti_3C_2T_x$ as anode materials for SIBs(13,42,43) have been experimentally studied on the electrochemical reaction mechanism. Nevertheless, the intrinsic lithium

storage mechanism of $Ti_3C_2T_x$ MXene remains to be experimentally unveiled, which limits not only the practical application of $Ti_3C_2T_x$ but also the property-oriented design of late-model electrode materials with superior performance.

Herein, to understand the intrinsic lithium storage mechanism of $Ti_3C_2T_x$ MXene, we apply ex situ X-ray diffraction (XRD) and operando electrochemical impedance spectroscopy (EIS) combined with density functional theory (DFT) calculations to investigate the structural and electrochemical behaviors of $Ti_3C_2T_x$ during the (de)intercalation process. It is demonstrated that the charge-storage of $Ti_3C_2T_x$ as an intercalation anode depends on terminal Ti, which is definitely evidenced by the fact that the transition metal atoms bonded with various surface groups undergo specific redox reactions at well-recognized voltages. We confirm the linkage between different interlayer slits leading to sequential Li-ion (de)intercalation and specific redox couples at well-recognized voltages. A zero-strain feature in $Ti_3C_2T_x$ upon Li-ion (de)intercalation was confirmed. Overall, we elucidate the Li-ion storage mechanism for MXene and provide the design principle.

2. Methods

2.1. Materials

Ti powders (99%, −300 mesh) were provided by Haixin (China), Al powders (99%, D_{50} = 10 μm) were obtained from AIFA (China), and graphite powders (99%, D_{90} = 6.5 μm) were purchased from TIMCAL (Switzerland). Ar (99.999%), Ar (5% H_2), and NH_3 (99.999%) were provided by Dalian Special Gases Co., LTD. Hydrofluoric acid (HF, 40%) and *N*-methyl-2-pyrrolidinone (NMP, 99.8%) were purchased from Sinopharm Chemical Reagent Co., LTD. Polyvinylidene fluoride (PVDF) was obtained from Alfa Aesar. All of the chemicals were used as received without further purification.

2.2. Synthesis of $Ti_3C_2T_x$ MXene

The Ti_3AlC_2 monolith for the synthesis of $Ti_3C_2T_x$ was prepared by the method reported previously.(44,45) Briefly, Ti_3AlC_2 was prepared by heating a mixture of Ti, Al, and C at 1400 °C for 1.5 h in an argon gas environment. The prepared porous monolith is phase pure as determined by XRD examination (Figure S1). $Ti_3C_2T_x$ was synthesized by etching 1.0 g of Ti_3AlC_2 in 6 mol L^{-1} HF aqueous solution (10 mL) for a week at room temperature. The resultant sediment was washed several times with deionized water until the pH reached 5. Finally, the washed sediment was separated by vacuum filtration, and dried at 60 °C for 12 h. The dried sediment in form of powders was collected for further use.

2.3. Calcination of $Ti_3C_2T_x$ MXene in Various Controlled Atmospheres

In a typical experiment for the preparation of Ar(H_2O)–$Ti_3C_2T_x$, 0.5 g of $Ti_3C_2T_x$ powders were loaded into a quartz tube furnace with an inner diameter of 36 mm. The sample chamber was degassed using a vacuum pump, and subsequently filled with a mixed flow of Ar(H_2O). To further remove the

residual atmosphere in the sample chamber, another degassing–filling procedure was repeated. The $Ti_3C_2T_x$ powders were then heated at a rate of 10 °C min^{-1} up to 400 °C. After 1 h-dwelling at that temperature, the sample was cooled down to room temperature under the protection of Ar(H_2O) mixed flow. The flow rate of the mixed flow was 100 sccm. The mixed flow of Ar(H_2O) was obtained by bubbling Ar flow through deionized water (Figure S2). According to the saturated vapor pressure of water(46) at 25 °C (3.169×10^3 Pa), the water content in the mixed flow of Ar(H_2O) is determined to be 3.1%. The other two types of $Ti_3C_2T_x$ MXene powders, Ar(H_2)–$Ti_3C_2T_x$ and NH_3–$Ti_3C_2T_x$, were prepared with the same calcination procedure, except that gas flow was replaced by Ar(H_2) and NH_3, respectively.

2.4. Materials Characterization

The phase purity and crystalline structure of the products were characterized by powder X-ray diffractometer (XRD, D/max-2400, Rigaku, Japan) with Cu Kα radiation (λ = 0.15418 nm). To investigate the Li^+ storage mechanism in the pristine–$Ti_3C_2T_x$ and NH_3–$Ti_3C_2T_x$ materials, ex situ XRD examinations were carried out on the pristine–$Ti_3C_2T_x$ and NH_3–$Ti_3C_2T_x$ electrodes that were charged or discharged at selected voltages. Coin batteries were disassembled in an Ar-filled glove box, and the electrodes were sealed in centrifuge tubes to protect them from ambience. The samples were immediately transferred to the analysis chamber of the XRD apparatus (XRD, D/max-2500, Rigaku, Japan). XRD data were collected from 5 to 65° of 2θ with a step of 0.04°. The surface morphology and microstructure of MXene samples were characterized on a field-emission scanning electron microscope (FESEM, LEO Supra 35, Zeiss). Brunauer–Emmett–Teller (BET) specific surface areas (SASs) (Micromeritics ASAP 2020) were measured with nitrogen as adsorption gas at 77 K. Transmission electron microscopy (TEM) characterization was done on a Tecnai G2 F20 FEI transmission electron microscope working at an accelerating voltage of 200 kV. The microscope is equipped with a Gatan charge-coupled device (CCD) camera. For the morphological purpose. TEM samples were made by depositing a drop of diluted suspension in ethanol on a carbon film-coated copper grid. Chemical compositions and oxidation state of the samples were further analyzed using high-resolution X-ray photoelectron spectroscopy (XPS) (ESCALAB250, Thermo VG) with monochromated Al Kα radiation (1486.6 eV). All binding energies were referenced to C 1s of free carbon (284.6 eV). Peak deconvolution was carried out using commercially available software, CasaXPS. A Raman spectrometer (LabRAM HR800, air-cooled CCD array detector, Horiba Jobin-Yvon, France) was applied to characterize the untreated and treated $Ti_3C_2T_x$ MXene. A He–Ne laser radiation source (632.82 nm) was focused to a spot size of ~2 μm using a power of around 8 mW. For atomistic-scale observations, TEM foils were sliced from the MXene particles perpendicular to the basal plane on FEI Nova NanoSEM 450 (FEI, Oregon) equipped with a dual-beam SEM/FIB system. High-angle annular dark-field scanning transmission electron microscopy (HAADF-STEM) images were

taken on a double-Cs-corrected FEI Titan 360–300 operating at 300 kV, using a collection of an inner semiangle of 50 mrad and a convergence semiangle of 21 mrad.

2.5. Electrochemical Measurement

For the preparation of the lithium ion battery anodes, 10 wt % Super P was first mixed with 10 wt % PVDF in NMP, followed by the addition of 80 wt % of the active material (pristine–$Ti_3C_2T_x$ Ar(H_2O)–$Ti_3C_2T_x$, Ar(H_2)–$Ti_3C_2T_x$, or NH_3–$Ti_3C_2T_x$). The mixture was mixed homogeneously in an agate mortar. The resultant slurry was pasted on a Cu foil and dried at 140 °C in an vacuum oven for 12 h. The 2025-type coin cells were then assembled in an argon-filled glove box using lithium foil as both the counter and reference electrode, Celgard 2600 as the separator, and 1 M $LiPF_6$ dissolved in ethylene carbonate and dimethyl carbonate with a volume ratio of 1:1 as the electrolyte. The assembled cells were galvanostatically cycled at various discharge and charge rates (1C = 320 mAh g^{-1}) in the voltage range of 0.05–3.0 V on a LAND CT2001A cycler (Wuhan Kingnuo Electronic Co., China). The cyclic voltammetry (CV) measurements were carried out using an electrochemical workstation (PARSTAT 2273, Princeton Applied Research) at various scan rates from 0.05 to 3.0 V. Electrochemical impedance spectroscopy (EIS) was conducted on an electrochemical workstation (PARSTAT 2273, Princeton Applied Research). The EIS spectra were recorded from 100 kHz to 10 mHz with an amplitude of 5 mV.

2.6. Computational Methods

Density functional theory computations were performed by using the Cambridge Sequential Total Energy Package. The electron–ion interaction was described by using the plane-wave pseudopotential. The exchange-correlation energy is described by the functional of GGA-PW91. The long-range interaction was considered by dispersion correction within the OBS methods. The cutoff energy was set to 380 eV. To investigate the effect of N-doping on MXene, a moderate concentration (1/16) carbon deficiency model is used by constructing a 2 × 2 × 1 $Ti_3C_2O_2$ supercell with N occupying carbon vacancy. The N-doped $Ti_3C_2O_2$ MXene was labeled as N@$Ti_3C_2O_2$. The carbon atom at the 1b Wyckoff position was removed. The detailed information of $Ti_3C_2O_2$ structural data can be obtained from supporting materials. The Brillouin zone was represented by a Monkhorst–Pack special *k*-point mesh of 5 × 5 × 1 for geometry optimizations. For electronic structure computations, all atoms were allowed to move until the energy was less than 10^{-5} eV per atom and the force on each atom was less than 0.05 eV $Å^{-1}$, a larger *k*-point mesh of 9 × 9 × 1 was used.

3. Results and Discussion

3.1. Morphological and Structural Investigations

Unlike the Ti_3AlC_2 powders commonly used as the precursor for preparing MXene, the porous Ti_3AlC_2 monolith was used in this work. The advantage of

using a porous monolith instead of powder is that the Ti_3AlC_2 grain integrity could be retained in the etched $Ti_3C_2T_x$ MXene,(44,45) which is confirmed by the morphological investigations of pristine $Ti_3C_2T_x$ by scanning electron microscopy (SEM). To modulate the surface/interface chemistry, the pristine $Ti_3C_2T_x$ powders were heat treated in three different atmospheres including Ar(H_2), Ar(H_2O), and NH_3, respectively. In this work, we focus on a moderate temperature of 400 °C.

Interestingly, heat treatment in the atmospheres leads to diverse changes in the apparent thickness of $Ti_3C_2T_x$ platelets. In the atmospheres of Ar(H_2) and Ar(H_2O), the thickness increased, whereas it decreased in NH_3 (Figure S3). Such changes were further identified by nitrogen adsorption/desorption isotherm types and the corresponding Brunauer–Emmett–Teller (BET) specific surface area and Barrette-Joynere-Halenda pore size distribution (Figures S4 and S5). Accordingly, Ar(H_2)–$Ti_3C_2T_x$, Ar(H_2O)–$Ti_3C_2T_x$, and pristine–$Ti_3C_2T_x$ have specific surface areas (SSAs) of 5.8, 4.2, and 3.0 $m^2\ g^{-1}$, respectively, whereas the SSA of NH_3–$Ti_3C_2T_x$ is only 1.4 $m^2\ g^{-1}$. On the basis of microstructural observations (Figure S3), it is demonstrated that all heat-treated samples retained identical crystal structure to the pristine one, which is further verified by the transmission electron microscopy (TEM) images and corresponding selected area electron diffraction patterns of pristine–$Ti_3C_2T_x$ and NH_3–$Ti_3C_2T_x$ (Figure S6).

To examine the phase composition, pristine $Ti_3C_2T_x$ along with those heat-treated in three different atmospheres was subjected to X-ray diffraction (XRD). It is important to note that there are two striking features in the XRD patterns (Figure 1). First, the XRD patterns of Ar(H_2)–$Ti_3C_2T_x$ and Ar(H_2O)–$Ti_3C_2T_x$ resemble the pristine one, whereas NH_3–$Ti_3C_2T_x$ differs significantly from its counterparts in terms of intensity. Moreover, the (002) reflection downshifts from 9.03° for the pristine–$Ti_3C_2T_x$ to 7.22°, indicating the increased interlayer spacing in NH_3–$Ti_3C_2T_x$. One possible explanation for the large interlayer distance is that nitrogen-containing species has been incorporated between the interlayers, which is verified by X-ray photoelectron spectroscopy (XPS). Second, there are recognizable reflections from anatase TiO_2 in Ar(H_2)–$Ti_3C_2T_x$ and Ar(H_2O)–$Ti_3C_2T_x$. The presence of anatase TiO_2 is evidenced by the characteristic redox couples in the cyclic voltammetry (CV) curves as detailed in the electrochemical evaluation in the discussion section.

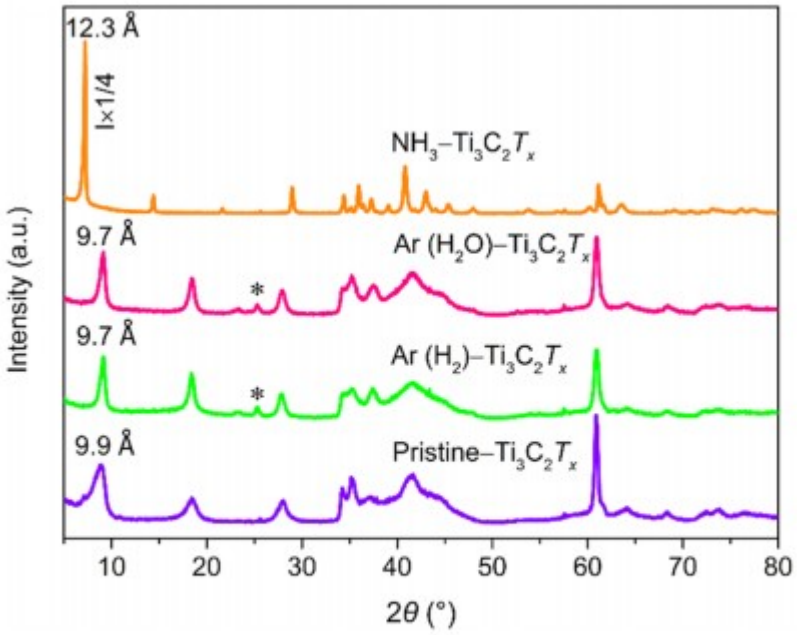

Figure 1. XRD patterns of pristine–$Ti_3C_2T_x$, Ar(H_2)–$Ti_3C_2T_x$, Ar(H_2O)–$Ti_3C_2T_x$, and NH_3–$Ti_3C_2T_x$. The asterisk corresponds to anatase TiO_2. The spacing of (002) reflection is indicated.

Consistent with the remarkable shift of (002) reflection in XRD patterns, high-angle annular dark-field scanning transmission electron microscopy (HAADF-STEM) images verify that the *c*-lattice parameter of pristine–$Ti_3C_2T_x$ is 19.8 Å and that of NH_3–$Ti_3C_2T_x$ is 24.5 Å. Regardless of pristine–$Ti_3C_2T_x$ or NH_3–$Ti_3C_2T_x$, light elements of the surface groups are less visible between the layers, but the distinction in spacing between the two samples is significant (Figure 2). Furthermore, the interlayer spacing observed in the HAADF-STEM image of the pristine–$Ti_3C_2T_x$ is nonuniform, whereas that of NH_3–$Ti_3C_2T_x$ is rather uniform with large interlayer spacing, which is consistent with XRD patterns (Figure 1).

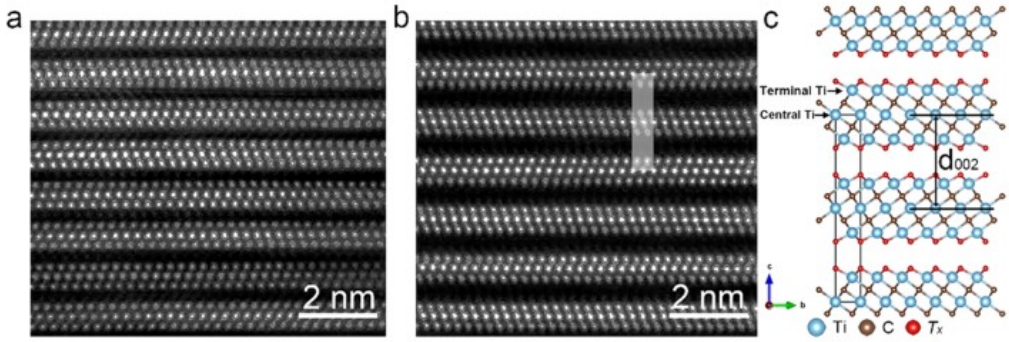

Figure 2. HAADF-STEM images of (a) pristine–$Ti_3C_2T_x$ and (b) NH_3–$Ti_3C_2T_x$, along the $[11\bar{2}0]$ zone axis.The rectangle corresponds to the single unit cell. (c) Atomistic configuration of $Ti_3C_2T_x$ with layered structure, showing terminal Ti, central Ti, and d_{002}.

3.2. Spectroscopic Characterization

It is generally acknowledged that heat treatment in the atmosphere would modify the surface/interface chemistry.(47) To study the chemistry of $Ti_3C_2T_x$ MXene after calcination in different atmospheres, Raman spectroscopic investigation was conducted. The Raman spectra of pristine $Ti_3C_2T_x$ MXene and those heat-treated are plotted in Figures 3a and S7. All samples investigated in this work generally show the characteristic vibrational modes for $Ti_3C_2T_x$ MXene.(47) In addition, compared with pristine–$Ti_3C_2T_x$, the calcined samples of NH_3–$Ti_3C_2T_x$, Ar(H_2)–$Ti_3C_2T_x$, and Ar(H_2O)–$Ti_3C_2T_x$ exhibit a low-intensity feature for the band at around 128 cm^{-1}, which is assigned to out-of-plane vibrations of C atoms in $Ti_3C_2F_2$.(47) Moreover, the spectra of NH_3–$Ti_3C_2T_x$, Ar(H_2)–$Ti_3C_2T_x$, and Ar(H_2O)–$Ti_3C_2T_x$ are more similar to $Ti_3C_2O_2$. These interesting results indicate that pristine–$Ti_3C_2T_x$ possesses more −F groups, whereas −F groups in the samples of Ar(H_2O)–$Ti_3C_2T_x$ and Ar(H_2)–$Ti_3C_2T_x$ were somewhat removed.(47) On the basis of the previous report, the mode at 730 cm^{-1} is assigned to out-of-plane vibrations of C atoms in $Ti_3C_2O_2$, and that at 708 cm^{-1} belongs to the out-of-plane vibrations of C atoms in $Ti_3C_2O(OH)$. Upon treatment in the three different atmospheres, the Raman band near 708 cm^{-1} shifts to higher frequencies, suggesting increased −O concentration of groups at the expense of dehydrogenation of −OH groups. (41) The above vibrational spectroscopic results are in excellent agreement with the electron spectroscopic investigations by XPS.

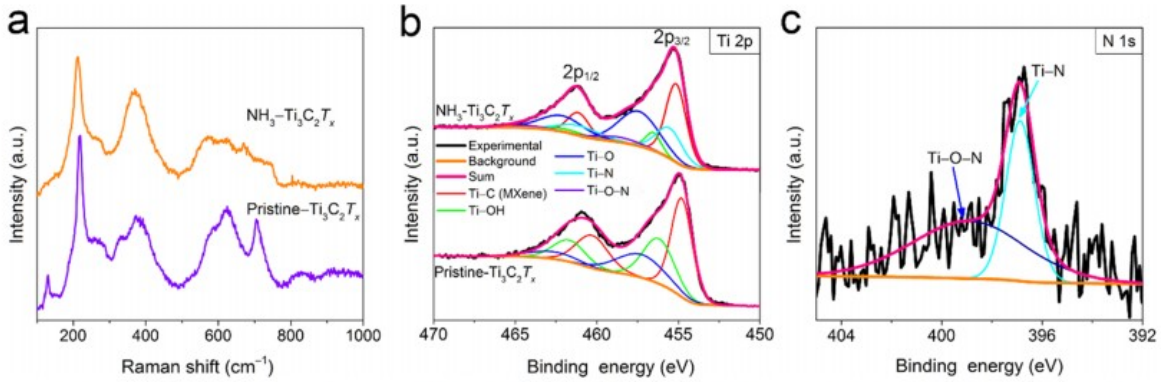

Figure 3. (a) Raman spectra of pristine−$Ti_3C_2T_x$ and NH_3−$Ti_3C_2T_x$. (b) Component peak-fitting of Ti 2p XPS spectra for pristine−$Ti_3C_2T_x$ and NH_3−$Ti_3C_2T_x$. Binding energy values of the deconvoluted peaks are listed in Table S3. (c) N 1s XPS spectrum of NH_3−$Ti_3C_2T_x$. The XPS spectra were recorded after Ar sputtering for 60 s.

According to the XPS survey spectra, four major elements of Ti, C, O, and F are detected in the pristine $Ti_3C_2T_x$ MXene and those heat-treated (Figure S8). It is obvious that heat treatment in ammonia introduces N element, which is consistent with the electron energy loss spectrum (Figure S9). Elemental compositions of the samples investigated in this study are summarized in Table S1. Based on Table S1, we can deduce that the quantity of −N groups in one $Ti_3C_2T_x$ unit is 0.33 for NH_3–$Ti_3C_2T_x$. Notably, irrespective of the atmosphere, calcination increases O concentration, whereas it decreases F concentration (Figure S10 and Table S2). These experimental

results agree with the theoretical studies that O-terminated MXene is the most stable species.(48,49)

Due to the two-dimensional nature, $Ti_3C_2T_x$ MXene is regarded as a combination of a central homoleptic Ti-centered octahedron and a surface heteroleptic Ti-centered octahedron.(48) Since the difference in the immediate environment of Ti atoms, referred to as central Ti and terminal Ti, the binding energies of electrons arising from Ti may be distinguished.(48) As shown in Figures 3b and S11, deconvolution of the Ti 2p spectrum of pristine–$Ti_3C_2T_x$ definitely demonstrates that the oxidation states of Ti are distinguished in terms of binding energy. Moreover, terminal Ti atoms correspond to a high oxidation state compared with central titanium.

From the N 1s spectrum of NH_3–$Ti_3C_2T_x$ (Figures 3c, S12 and Table S4), the present state of N could be identified. There are two distinct N 1s peaks in the XPS spectrum of NH_3–$Ti_3C_2T_x$. Importantly, the intensity of the peak at 397 eV depends much on sputtering time whereas that of the peak at ∼399.6 eV does not (Figure S12). Based on this important information, the former binding energy is reasonably ascribed to chemisorbed γ-N_2(50) from ambience, and the latter corresponds to Ti–N and/or Ti–O–N(29,51,52) of the MXene. We know that carbon vacancy is a common phenomenon in the experimentally prepared MXene.(53−55) Hence, N-doping in the carbon vacancy is reasonable, which has been verified by theoretical DFT calculations.

3.3. Theoretical DFT Calculations

To further understand the effect of N doping on the electronic structure of $Ti_3C_2T_x$, DFT calculations were performed with the N atom occupying the carbon vacancy. $Ti_3C_2O_2$ was selected as a model since −O termination is the dominant surface functional group after treatment in an ammonia atmosphere. So the pristine $Ti_3C_2T_x$ also used the formula of $Ti_3C_2O_2$ for the sake of comparison. The related density of states (DOS) of the pristine $Ti_3C_2O_2$ and N doped $Ti_3C_2O_2$ are also compared. In all cases investigated, regardless of configuration, the substantial DOSs at the Fermi level (E_F) are all dominated by Ti 3d orbitals, as shown in Figure S13. In addition, similar trends and shapes in the vicinity of E_F are observed, indicating that N doping in $Ti_3C_2O_2$ has no obvious enhancement in the electrical conductivity of the material. Structural relaxation and formation energy calculations indicate that N-doped $Ti_3C_2O_2$ MXene can exist (Table S5). In the case of pristine–$Ti_3C_2T_x$ bearing a carbon vacancy, there is a possibility of Li occupying the carbon vacancy. Whether the carbon vacancy in MXene can serve as a host of intercalated Li ions is another important issue. Here, we checked the possibility of carbon-deficient $Ti_3C_2O_2$ to accommodate Li ions. Surprisingly, O-terminated $Ti_3C_2T_x$ MXene, the thermionically most stable species, after Li ions occupying carbon vacancy, becomes unstable. The Li ions occupying the carbon vacancy lead to significant volume expansion accompanied by Ti–C bond breaking, which results in the disruption of the structural integrity

(Figure S14). These results demonstrate that the carbon vacancy in $Ti_3C_2T_x$ is unlikely to contribute to reversible Li ion storage. Thus, it is reasonable to assume that the storage of Li ions occur only between the interlayers of $Ti_3C_2T_x$ MXene.

3.4. Electrochemical Evaluation

Having firmly demonstrated the structural features of pristine–$Ti_3C_2T_x$, Ar(H_2)–$Ti_3C_2T_x$, Ar(H_2O)–$Ti_3C_2T_x$, and NH_3–$Ti_3C_2T_x$, we evaluated their electrochemical properties by means of cyclic voltammetry (CV) and operando electrochemical impedance spectroscopy (EIS), to understand the lithium storage mechanism of $Ti_3C_2T_x$ MXene.

CV is a versatile electroanalytical technique for the study of electroactive species. The effectiveness of CV results from its capability for rapidly observing the redox behavior over a wide potential range.(56) We conducted CV measurements to clarify the influence of changing surface groups on electrochemical behaviors. Strikingly, treatment in the atmospheres leads to different changes in the electrochemical reaction. First, two redox couples near 2.53/2.45 and 1.00/0.97 V in the pristine–$Ti_3C_2T_x$ electrode are observed. Compared with pristine–$Ti_3C_2T_x$, an additional redox couple appears in the sample of Ar(H_2)–$Ti_3C_2T_x$ and Ar(H_2O)–$Ti_3C_2T_x$ electrodes. In contrast, there is only one redox couple in NH_3–$Ti_3C_2T_x$ (Figure 4). The shape of CV curves and position of redox couples of Ar(H_2)–$Ti_3C_2T_x$ and Ar(H_2O)–$Ti_3C_2T_x$ electrodes resemble those of the pristine–$Ti_3C_2T_x$ electrode except for a redox couple near 2.05/1.71 V corresponding to the characteristics of anatase TiO_2(57,58) that has been verified by XRD (Figure 1). Therefore, we focus on pristine–$Ti_3C_2T_x$ and NH_3–$Ti_3C_2T_x$ in the following discussion. As aforementioned, the biggest difference between these two samples is that pristine–$Ti_3C_2T_x$ has two redox couples, whereas NH_3–$Ti_3C_2T_x$ has only one. A possible explanation for this interesting difference is that Li-ion (de)intercalation between interlayers of the pristine–$Ti_3C_2T_x$ electrode is in a sequential manner, whereas NH_3–$Ti_3C_2T_x$ undergoes a simultaneous Li-ion (de)intercalation. To track the evolution of interlayer spacing upon charging/discharging, we conducted carefully ex situ XRD investigations.

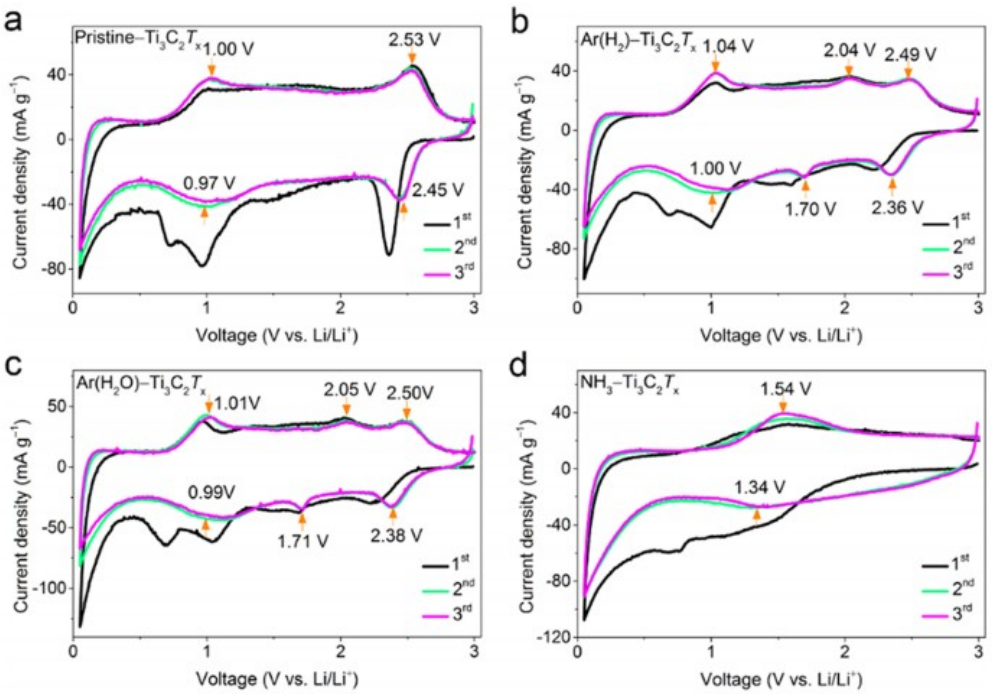

Figure 4. CV curves of (a) pristine–$Ti_3C_2T_x$, (b) $Ar(H_2)$–$Ti_3C_2T_x$, (c) $Ar(H_2O)$–$Ti_3C_2T_x$, and (d) NH_3–$Ti_3C_2T_x$ at a scan rate of 0.1 mV s^{-1} (the first three cycles).

In general, Li-ion (de)intercalation into electrode materials leads to structural change during the charging and discharging process.(59) To study the lithium storage mechanism of $Ti_3C_2T_x$, we conducted carefully ex situ XRD measurements on the electrode materials that were charged or discharged at selected cell voltages (Figure 5). Very interestingly, the XRD diffraction peaks remain the same in the whole range of charge/discharge voltage, indicating a zero-strain feature. It is deserved to point out that the electrode materials alerted somewhat due to possible spontaneous penetration of the electrolyte(60) during contact with the electrolyte as assembled in the coin cell, which is confirmed by the XRD patterns (Figure S17, Tables S6 and S7). Strikingly, two diffraction peaks are recognized in the (002) peak region of pristine–$Ti_3C_2T_x$ after the third charge/discharge cycle. We distinguish the two peaks as the high-angle peak corresponding to small interlayer slits and the low-angle peak corresponding to large interlayer slits. From Figures S18 and S19, the peak areas vary regularly with the extent of Li-ion (de)intercalation at different voltages. We first focus on the discharge process. From point A to point B, the low-angle peak area decreases as the discharge voltage decreases from 3.0 to 2.2 V. Similarly, when the voltage decreases from 1.5 to 0.6 V (point C → D), the high-angle peak area also shrinks.(61) Recalling the CV curve (Figure 4a), there are two obvious reduction peaks in the two regions (point A → B and point C → D), where diffusion-controlled Li-ion intercalation occurs.(62) When Li ions are intercalated into the interlayer slits, the $Ti_3C_2T_x$ layers would corrugate, giving rise to a decreased diffraction peak area.(63) Therefore, it is suggested that Li-ion first intercalated into large interlayer slits and then intercalated into small interlayer slits. During

the charging process, the peak area increases with the charging voltage from 0.5 to 1.3 V (point F → G), and the peak area increases with the charging voltage from 2.1 to 3.0 V (point H → I). Combined with the CV profile, there are two well-recognized oxidation peaks in two ranges (point F → G and point H → I), where diffusion-controlled Li-ion deintercalation occurs.(62) Therefore, lithium ions preferentially deintercalate from large interlayer slits after small interlayer slits.

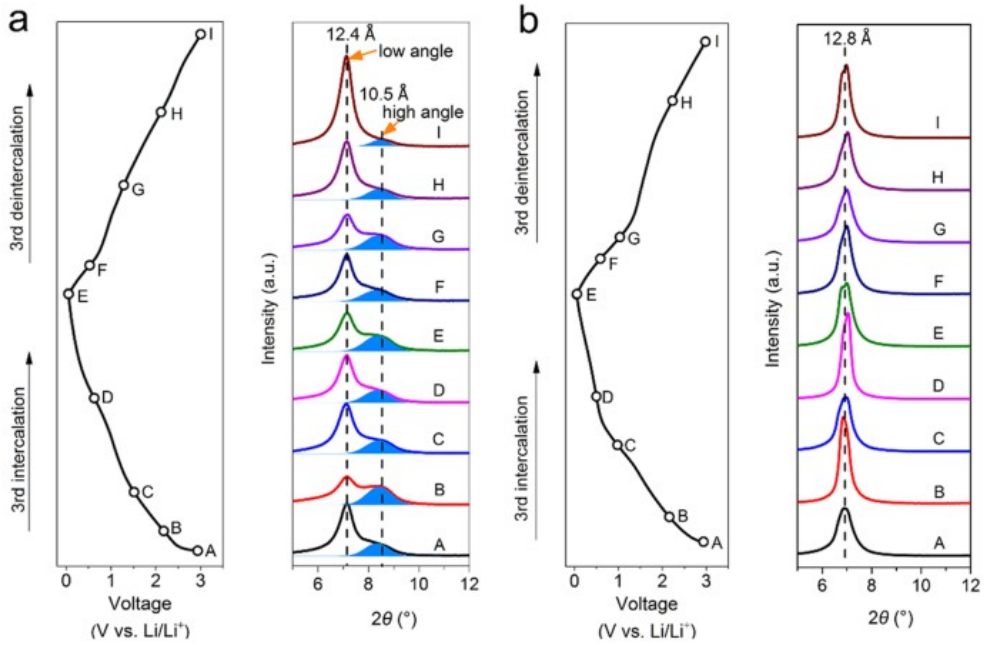

Figure 5. (a) Ex situ XRD patterns (right panel) for pristine−$Ti_3C_2T_x$ upon electrochemical (de)intercalation cycling (left panel). Note that two peaks in pristine−$Ti_3C_2T_x$ are well-defined with a low-angle peak and a high-angle peak, corresponding to *d*-spacing values of 12.4 and 10.5 Å, respectively. (b) Ex situ XRD patterns (right panel) for NH_3−$Ti_3C_2T_x$ upon electrochemical (de)intercalation cycling (left panel). Note that one peak in NH_3−$Ti_3C_2T_x$ is observed with a *d*-spacing of 12.8 Å.

We define the process of Li ion (de)intercalation between large and small interlayer slits as sequential lithium storage. Specifically, Li ions preferentially intercalate into large interlayer slits and then small interlayer slits, whereas Li ions first deintercalate from small interlayer slits and then large interlayer slits. The sequential (de)intercalation behavior of Li ions in two distinct interlayer slits excellently coincides with the redox couples exhibited on the CV profile. Unlike pristine–$Ti_3C_2T_x$, NH_3–$Ti_3C_2T_x$ has a uniform and large interlayer spacing, which leads to one redox couple on the CV curves upon Li ion (de)intercalation. This fact once again supports the viewpoint that the Li ion (de)intercalation between MXene interlayers undergoes in a sequential feature once there are distinct interlayer spacings. Reversible Li-ion (de)intercalation in the interlayer spacing as well as zero-strain (de)intercalation is advantageous to the high-rate capability.(64) Even sodium ion with larger ionic radius (de)intercalation into $Ti_3C_2T_x$, as reported by Yamada and co-workers,(43) has not undergone remarkable structural changes. This may be due to the stronger interlayer coupling of $Ti_3C_2T_x$

MXene(65) than the typical two-dimensional materials like graphite in which the interlayers are coupled via van der Waals force.

EIS is a well-known technique to understand the overall electrode properties and the electrochemical changes that occur within the electrode.(66) To unveil what is going on in the cell during the discharge–charge process, operando EIS investigations were taken at different specific voltages focusing on pristine–$Ti_3C_2T_x$ and NH_3–$Ti_3C_2T_x$, as shown in Figure 6. The EIS of the pristine–$Ti_3C_2T_x$ electrode consists of two depressed semicircles at high- and medium-frequency domains, respectively, and a straight line at the low frequency region. The two depressed semicircles are related mainly to lithium ion migration through the SEI films (R_{SEI}), and charge transfer at the SEI films/active material interface (R_{ct}), respectively.(63) The impedance spectrum at the redox peak position of 2.4 V comprises an additional arc. This is indicative of additional impedance that can therefore be ascribed to the migration of lithium ions between the MXene interlayer (R_m). Interestingly, there are pronounced differences in the parameters (R_{ct} and R_m) between pristine–$Ti_3C_2T_x$ and NH_3–$Ti_3C_2T_x$. According to the simulation results of the EIS spectra (Tables S8 and S9), the arc diameters of NH_3–$Ti_3C_2T_x$ related to R_m at different voltages are smaller than those of pristine–$Ti_3C_2T_x$. A possible explanation for the difference in R_m between pristine–$Ti_3C_2T_x$ and NH_3–$Ti_3C_2T_x$ is that large and uniform interlayer slits are beneficial to the migration of lithium ions therein. This was also reflected in the XRD patterns and STEM images, as well as in the CV curves. Moreover, the charging process is similar to that of the discharging process (Figure S20, Tables S10, and S11).

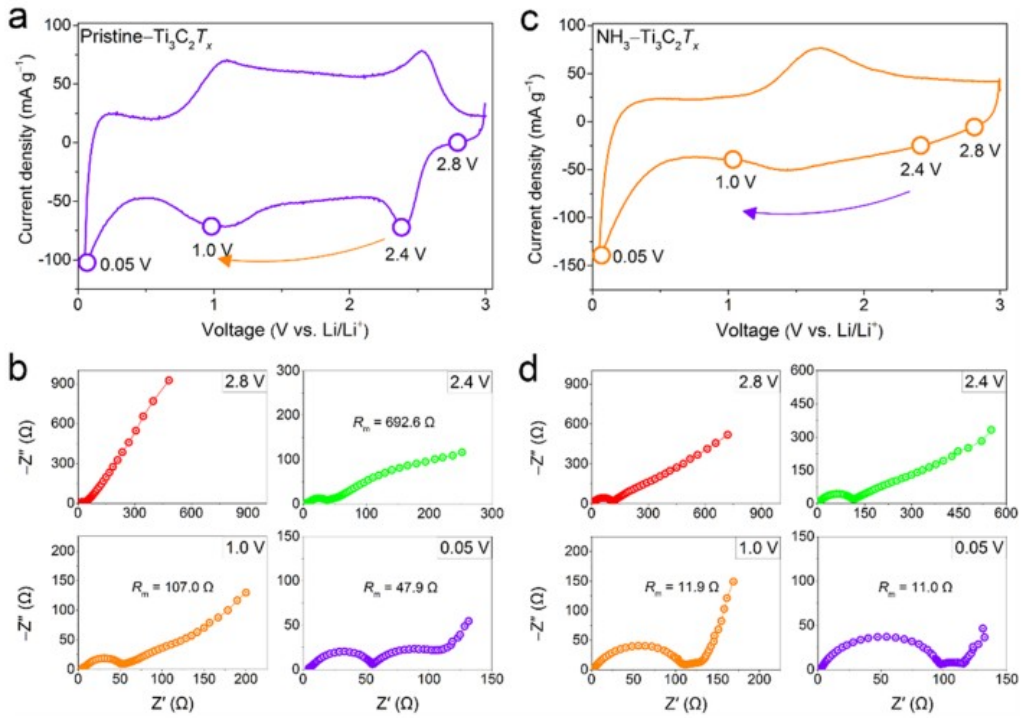

Figure 6. Comparing pristine–$Ti_3C_2T_x$ and NH_3–$Ti_3C_2T_x$ electrodes at various predetermined voltages using CV and operando EIS (Nyquist plots).(a) CV profile of pristine–$Ti_3C_2T_x$ recorded at a rate of 0.2 mV s^{-1}. Specific voltages at which operando EIS spectra are indicated. (b) Operando EIS (Nyquist plots) spectra of pristine–$Ti_3C_2T_x$ at predetermined voltages. (c) CV profile of NH_3–$Ti_3C_2T_x$ recorded at a rate of 0.2 mV s^{-1}. Specific voltages at which operando EIS spectra are indicated. (d) Operando EIS (Nyquist plots) spectra of NH_3–$Ti_3C_2T_x$ at predetermined voltages.

A comparison of the rate performances between pristine–$Ti_3C_2T_x$ and NH_3–$Ti_3C_2T_x$ shows that surface functionalization by NH_3 enhanced its performance especially at various rates ranging from 0.1C to 2C, whereas the capacity of NH_3–$Ti_3C_2T_x$ electrodes has no advantage at high rates (5C–10C), which could be ascribed to the combined effect of capacitance contribution and diffusion–limited contribution (Figures 7 and S21). At low rates, a diffusion–limited process is a major contributor to capacity, whereas the capacitive effect limited process is dominant. Thus, all electrodes exhibit a more capacitive behavior with less contribution from Li-ion intercalation-related charge transfer reactions, leading to a similar capacity at high rates, which can be verified from the following kinetic analysis. Moreover, the NH_3–$Ti_3C_2T_x$ electrode showed good stability, in addition to the consistently highest capacity, among the pristine $Ti_3C_2T_x$ MXene and those heat-treated (Figures 7, S22, and S23). It can be found that the first cycle Coulombic efficiency of pristine $Ti_3C_2T_x$ is around 58%. The first cycle Coulombic efficiency of those heat-treated $Ti_3C_2T_x$ MXene has enhanced (63% for Ar(H_2)–$Ti_3C_2T_x$, 62% for Ar(H_2O)–$Ti_3C_2T_x$, and 64% for NH_3–$Ti_3C_2T_x$) due to the removal of some surface groups (−F and −OH). For NH_3–$Ti_3C_2T_x$, the capacity of 168 mAh g^{-1} corresponds to the uptake of 1.25 Li-ion per formula unit, whereas pristine–$Ti_3C_2T_x$ can host up to 0.75 mol of lithium and deliver a capacity of 100 mAh g^{-1} (per formula unit of $Ti_3C_2O_2$).

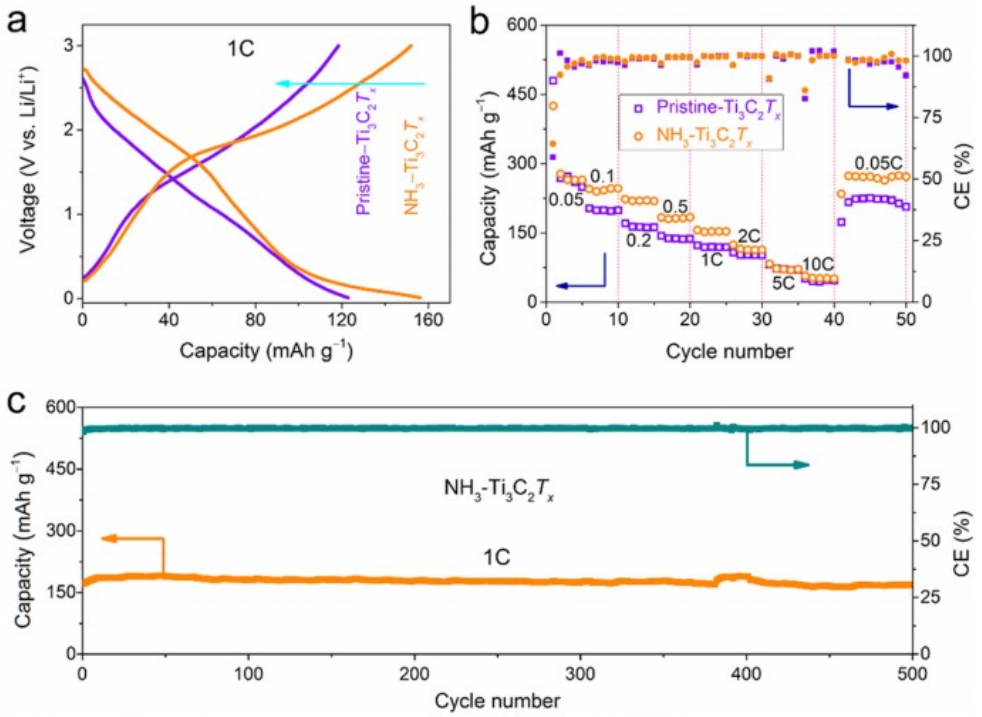

Figure 7. (a) Galvanostatic charge/discharge profiles at a current rate of 320 mA g^{-1} (1C). (b) Rate performances at various rates from 0.05C to 10C. (c) Long-term cycling performances of NH_3−$Ti_3C_2T_x$ at 1C. CE represents Coulombic efficiency.

The NH_3–$Ti_3C_2T_x$ electrode exhibits superior capacity over pristine–$Ti_3C_2T_x$ only at low rates (0.1C–2C), which contradicts its large interlayer spacing. To understand this interesting rate-dependent kinetic phenomenon, a comprehensive investigation by means of CV was conducted. The CV profiles recorded at scan rates from 0.1 to 2 mV s^{-1} are presented in Figures 8 and S24. Unlike the pristine–$Ti_3C_2T_x$ with two distinct redox couples, the NH_3–$Ti_3C_2T_x$ shows only one redox couple characterized by one broad anodic peak and a broader cathodic peak. Generally, there are three charge storage components in the charge storage process: the diffusion-controlled faradaic contribution from intercalation reaction, the faradaic contribution from charge transfer with surface/subsurface atoms (that is, the extrinsic pseudocapacitance effect), and the nonfaradaic contribution from the electrical double-layer effect.(67−69) The degree of capacitive effect can be qualitatively analyzed according to the relationship between measured current (i) and scan rate (v) from the CV profiles$i = av^b$(1)where a and b are fitting parameters. By plotting log(i) against log(v), we can obtain b-values from the slopes. Generally, a b-value of 0.5 (1) indicates a diffusion (capacitance)-controlled lithium storage process.(57,70,71) By plotting log(i) versus log(v), as shown in Figure 8b, b-values determined as the slopes are 0.87 and 0.78 corresponding to cathodic and anodic peaks, respectively. These two b-values are between 0.5 and 1, indicating that the charge storage is controlled by both the capacitance-dominated process and diffusion-controlled process.

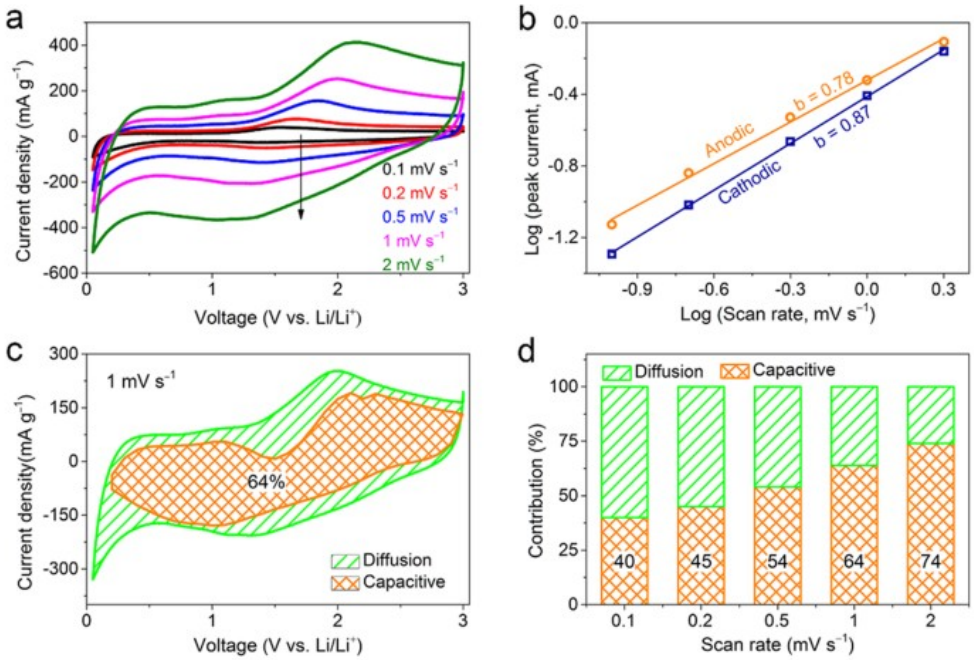

Figure 8. Kinetics analysis of the electrochemical bahavior toward Li ions for the NH_3–$Ti_3C_2T_x$ electrode. (a) CV curves of the NH_3–$Ti_3C_2T_x$ electrode at various scan rates from 0.1 to 2 mV s^{-1}. (b) Determination of the slope-value using the relationship between peak current and scan rate. (c) Determination of capacitive contribution from the CV data. (d) Contribution percentage of capacitive (orange) and diffusion-controlled (green) capacities at different rates for NH_3–$Ti_3C_2T_x$.

The current response (i) at a fixed potential (V) can be described as the combination of two separate mechanisms, namely the capacitive effect (k_1v) and diffusion-controlled process ($k_2v^{1/2}$) according to the equation(70,71)

$$i(V) = k_1v + k_2v^{1/2} \quad (2)$$

where v is the scan rate. Solving for the values of k_1 and k_2 at each potential allows for the separation of the diffusion and capacitive currents. On the basis of the quantitative analysis, the capacitive contributions of NH_3–$Ti_3C_2T_x$ monotonically increase upon increasing the scan rate. At a scan rate of 0.1 mV s^{-1}, the capacitive contribution percentage is only 40% whereas it increases to 74% at the scan rate of 2 mV s^{-1} (Figures 8c and S24a). Similarly, the capacitive contribution percentage of pristine–$Ti_3C_2T_x$ is also highly scan rate-dependent. This interesting scan rate-dependent capacitive contribution percentage unambiguously demonstrates that the capacitive contribution should play a critical role at high rates for the intercalation electrode materials like $Ti_3C_2T_x$ MXene. Based on the above discussion, reducing the lateral grain size is a rational synthetic strategy for further improving the rate capability of $Ti_3C_2T_x$ MXene through shortening the Li-ion diffusion path. Recently, submicron-sized or even nanosized $Ti_3C_2T_x$ was synthesized via a molten salt route in our laboratory.(72) The synthesis of submicron-sized or even nanosized $Ti_3C_2T_x$ offers a great opportunity for investigating the lateral size effect on rate capability. As demonstrated by rate capability evaluations (Figure S25), the submicron-sized $Ti_3C_2T_x$ synthesized actually exhibits superior rate performance over the pristine–

$Ti_3C_2T_x$ with a lateral size of tens of microns. This substantial result readily supports that reducing the lateral grain size of MXenes is definitely an applicable design principle for high-rate-capability electrode materials based on MXenes.

4. Conclusions

In summary, via detailed electrochemical, structural, kinetic, and spectroscopic studies, in tandem with DFT calculations, we provide in-depth insights into $Ti_3C_2T_x$ as an intercalation anode material that stores charge highly depending on the terminal Ti atom. This is definitely evidenced by the fact that the transition metal bonded with various surface groups undergoes specific redox reactions at well-recognized voltages. We confirm the linkage between different interlayer slits leading to sequential Li-ion (de)intercalation and specific redox couples at well-recognized voltages. We also confirm a zero-strain feature in $Ti_3C_2T_x$ upon Li-ion (de)intercalation. Overall, we elucidate the Li-ion storage mechanism for MXene and provide the design principle. We believe that these fundamental insights into Li-ion storage mechanism will guide the community to steer the optimization and development of MXene anodes and as such will hasten commercialization of high capacity MXene Li-ion batteries.

Acknowledgments

This work was supported by the Youth Innovation Promotion Association, Chinese Academy of Sciences (CAS), under grant No. 2011152, the Shenyang National Laboratory for Materials Science, Institute of Metal Research, CAS under grant No. 2017RP06, and the Special Program for Applied Research on Super Computation of the NSFC-Guangdong Joint Fund (the second phase) under Grant No. U1501501.

References

(1) Armand, M.; Tarascon, J. M. Building Better Batteries. Nature 2008, 451, No. 652.

(2) Etacheri, V.; Marom, R.; Elazari, R.; Salitra, G.; Aurbach, D. Challenges in the Development of Advanced Li-Ion Batteries: a Review. Energy Environ. Sci. 2011, 4, 3243−3262.

(3) Billaud, D.; McRae, E.; Herold, A. Synthesis and Electrical´ Resistivity of Lithium-Pyrographite Intercalation Compounds (stages I, II and III). Mater. Res. Bull. 1979, 14, 857−864.

(4) Song, X. Y.; Kinoshita, K.; Tran, T. D. Microstructural Characterization of Lithiated Graphite. J. Electrochem. Soc. 1996, 143, L120−L123.

(5) Wang, J.; Ren, Y.; Huang, X.; Ding, J. Inverse Spinel Transition Metal Oxides for Lithium-Ion Storage with Different Discharge/ Charge Conversion Mechanisms. Electrochim. Acta 2016, 219, 10−19.

(6) Jung, H.-G.; Myung, S.-T.; Yoon, C. S.; Son, S.-B.; Oh, K. H.; Amine, K.; Scrosati, B.; Sun, Y.-K. Microscale Spherical CarbonCoated Li4Ti5O12 as Ultra High Power Anode Material for Lithium Batteries. Energy Environ. Sci. 2011, 4, 1345−1351.

(7) Park, K.-S.; Benayad, A.; Kang, D.-J.; Doo, S.-G. NitridationDriven Conductive Li4Ti5O12 for Lithium Ion Batteries. J. Am. Chem. Soc. 2008, 130, 14930−14931.

(8) Shen, L.; Uchaker, E.; Zhang, X.; Cao, G. Hydrogenated Li4Ti5O12 Nanowire Arrays for High Rate Lithium Ion Batteries. Adv. Mater. 2012, 24, 6502−6506.

(9) Wang, H.; Wu, Y.; Yuan, X.; Zeng, G.; Zhou, J.; Wang, X.; Chew, J. W. Clay-Inspired MXene-Based Electrochemical Devices and Photo-Electrocatalyst: State-of-the-Art Progresses and Challenges. Adv. Mater. 2018, 30, No. 1704561.

(10) Xie, Y.; Naguib, M.; Mochalin, V. N.; Barsoum, M. W.; Gogotsi, Y.; Yu, X.; Nam, K.-W.; Yang, X.-Q.; Kolesnikov, A. I.; Kent, P. R. C. Role of Surface Structure on Li-Ion Energy Storage Capacity of TwoDimensional Transition-Metal Carbides. J. Am. Chem. Soc. 2014, 136, 6385−6394.

(11) Anasori, B.; Xie, Y.; Beidaghi, M.; Lu, J.; Hosler, B. C.; Hultman, L.; Kent, P. R. C.; Gogotsi, Y.; Barsoum, M. W. TwoDimensional, Ordered, Double Transition Metals Carbides (MXenes). ACS Nano 2015, 9, 9507−9516.

(12) Anasori, B.; Lukatskaya, M. R.; Gogotsi, Y. 2D Metal Carbides and Nitrides (MXenes) for Energy Storage. Nat. Rev. Mater. 2017, 2, No. 16098.

(13) Bak, S.-M.; Qiao, R.; Yang, W.; Lee, S.; Yu, X.; Anasori, B.; Lee, H.; Gogotsi, Y.; Yang, X.-Q. Na-Ion Intercalation and Charge Storage Mechanism in 2D Vanadium Carbide. Adv. Energy Mater. 2017, 7, No. 1700959.

(14) Naguib, M.; Come, J.; Dyatkin, B.; Presser, V.; Taberna, P.-L.; Simon, P.; Barsoum, M. W.; Gogotsi, Y. MXene: a Promising Transition Metal Carbide Anode for Lithium-Ion Batteries. Electrochem. Commun. 2012, 16, 61−64.

(15) Liu, Y.-T.; Zhang, P.; Sun, N.; Anasori, B.; Zhu, Q.-Z.; Liu, H.; Gogotsi, Y.; Xu, B. Self-Assembly of Transition Metal Oxide Nanostructures on MXene Nanosheets for Fast and Stable Lithium Storage. Adv. Mater. 2018, 30, No. 1707334.

(16) Wang, C.; Xie, H.; Chen, S.; Ge, B.; Liu, D.; Wu, C.; Xu, W.; Chu, W.; Babu, G.; Ajayan, P. M.; et al. Atomic Cobalt Covalently Engineered Interlayers for Superior Lithium-Ion Storage. Adv. Mater. 2018, 30, No. 1802525.

(17) Zhao, M.-Q.; Xie, X.; Ren, C. E.; Makaryan, T.; Anasori, B.; Wang, G.; Gogotsi, Y. Hollow MXene Spheres and 3D Macroporous MXene Frameworks for Na-Ion Storage. Adv. Mater. 2017, 29, No. 1702410.

(18) Xie, X.; Zhao, M.-Q.; Anasori, B.; Maleski, K.; Ren, C. E.; Li, J.; Byles, B. W.; Pomerantseva, E.; Wang, G.; Gogotsi, Y. Porous Heterostructured MXene/ Carbon Nanotube Composite Paper with High Volumetric Capacity for Sodium-Based Energy Storage Devices. Nano Energy 2016, 26, 513−523.

(19) Li, J.; Yan, D.; Hou, S.; Li, Y.; Lu, T.; Yao, Y.; Pan, L. Improved Sodium-Ion Storage Performance of Ti3C2Tx MXenes by Sulfur Doping. J.Mater. Chem. A 2018, 6, 1234−1243.

(20) Bao, W.; Liu, L.; Wang, C.; Choi, S.; Wang, D.; Wang, G. Facile Synthesis of Crumpled Nitrogen-Doped MXene Nanosheets as a New Sulfur Host for Lithium−Sulfur Batteries. Adv. Energy Mater. 2018, 8, No. 1702485.

(21) Liang, X.; Rangom, Y.; Kwok, C. Y.; Pang, Q.; Nazar, L. F. Interwoven MXene Nanosheet/Carbon-Nanotube Composites as Li− S Cathode Hosts. Adv. Mater. 2016, 29, No. 1603040.

(22) Liang, X.; Garsuch, A.; Nazar, L. F. Sulfur Cathodes Based on Conductive MXene Nanosheets for High-Performance Lithium− Sulfur Batteries. Angew. Chem., Int. Ed. 2015, 127, 3979−3983.

(23) Lin, C.; Zhang, W.; Wang, L.; Wang, Z.; Zhao, W.; Duan, W.; Zhao, Z.; Liu, B.; Jin, J. A Few-Layered Ti3C2 Nanosheet/Glass Fiber Composite Separator as a Lithium Polysulphide Reservoir for HighPerformance Lithium−Sulfur Batteries. J. Mater. Chem. A 2016, 4, 5993−5998.

(24) Ghidiu, M.; Lukatskaya, M. R.; Zhao, M.-Q.; Gogotsi, Y.; Barsoum, M. W. Conductive Two-Dimensional Titanium Carbide ‘Clay’ with High Volumetric Capacitance. Nature 2014, 516, No. 78.

(25) Lukatskaya, M. R.; Mashtalir, O.; Ren, C. E.; Dall’Agnese, Y.; Rozier, P.; Taberna, P. L.; Naguib, M.; Simon, P.; Barsoum, M. W.; Gogotsi, Y. Cation Intercalation and High Volumetric Capacitance of Two-Dimensional Titanium Carbide. Science 2013, 341, No. 1502.

(26) Zhang, C.; Kremer, M. P.; Seral-Ascaso, A.; Park, S.-H.; McEvoy, N.; Anasori, B.; Gogotsi, Y.; Nicolosi, V. Stamping of Flexible, Coplanar Micro-Supercapacitors Using MXene Inks. Adv. Funct. Mater. 2018, 28, No. 1705506.

(27) Rakhi, R. B.; Ahmed, B.; Hedhili, M. N.; Anjum, D. H.; Alshareef, H. N. Effect of Postetch Annealing Gas Composition on the Structural and Electrochemical Properties of Ti2CTx MXene Electrodes for Supercapacitor Applications. Chem. Mater. 2015, 27, 5314−5323.

(28) Zhang, C.; Kim, S. J.; Ghidiu, M.; Zhao, M.-Q.; Barsoum, M. W.; Nicolosi, V.; Gogotsi, Y. Layered Orthorhombic Nb2O5@ Nb4C3Tx and TiO2@Ti3C2Tx Hierarchical Composites for High Performance Li-Ion Batteries. Adv. Funct. Mater. 2016, 26, 4143− 4151.

(29) Wen, Y.; Rufford, T. E.; Chen, X.; Li, N.; Lyu, M.; Dai, L.; Wang, L. Nitrogen-Doped Ti3C2Tx MXene Electrodes for HighPerformance Supercapacitors. Nano Energy 2017, 38, 368−376.

(30) Urbankowski, P.; Anasori, B.; Hantanasirisakul, K.; Yang, L.; Zhang, L.; Haines, B.; May, S. J.; Billinge, S. J. L.; Gogotsi, Y. 2D Molybdenum and Vanadium Nitrides Synthesized by Ammoniation of 2D Transition Metal Carbides (MXenes). Nanoscale 2017, 9, 17722− 17730.

(31) Luo, J.; Zhang, W.; Yuan, H.; Jin, C.; Zhang, L.; Huang, H.; Liang, C.; Xia, Y.; Zhang, J.; Gan, Y.; et al. Pillared Structure Design of MXene with Ultralarge Interlayer Spacing for High-Performance Lithium-Ion Capacitors. ACS Nano 2017, 11, 2459−2469.

(32) Yao, H.; Zhang, F.; Zhang, G.; Luo, H.; Liu, L.; Shen, M.; Yang, Y. A Novel Two-Dimensional Coordination Polymer-Polypyrrole Hybrid Material as a High-Performance Electrode for Flexible Supercapacitor. Chem. Eng. J. 2018, 334, 2547−2557.

(33) Boota, M.; Anasori, B.; Voigt, C.; Zhao, M.-Q.; Barsoum, M. W.; Gogotsi, Y. Pseudocapacitive Electrodes Produced by OxidantFree Polymerization of Pyrrole between the Layers of 2D Titanium Carbide (MXene). Adv. Mater. 2015, 28, 1517−1522.

(34) Zheng, W.; Zhang, P.; Chen, J.; Tian, W. B.; Zhang, Y. M.; Sun, Z. M. In Situ Synthesis of CNTs@Ti3C2 Hybrid Structures by Microwave Irradiation for High-Performance Anodes in Lithium Ion Batteries. J. Mater. Chem. A 2018, 6, 3543−3551.

(35) Yu, P.; Cao, G.; Yi, S.; Zhang, X.; Li, C.; Sun, X.; Wang, K.; Ma, Y. Binder-Free 2D Titanium Carbide (MXene)/Carbon Nanotube Composites for High-Performance Lithium-Ion Capacitors. Nanoscale 2018, 10, 5906−5913.

(36) Tang, H.; Zhuang, S.; Bao, Z.; Lao, C.; Mei, Y. Two-Step Oxidation of MXene in the Synthesis of Layer-Stacked Anatase Titania with Enhanced Lithium-Storage Performance. ChemElectroChem 2016, 3, 871−876.

(37) Guo, X.; Xie, X.; Choi, S.; Zhao, Y.; Liu, H.; Wang, C.; Chang, S.; Wang, G. Sb2O3/MXene(Ti3C2Tx) Hybrid Anode Materials with Enhanced Performance for Sodium-Ion Batteries. J. Mater. Chem. A 2017, 5, 12445−12452.

(38) Chen, C.; Xie, X.; Anasori, B.; Sarycheva, A.; Makaryan, T.; Zhao, M.; Urbankowski, P.; Miao, L.; Jiang, J.; Gogotsi, Y. MoS2-onMXene Heterostructures as Highly Reversible Anode Materials for Lithium-Ion Batteries. Angew. Chem., Int. Ed. 2018, 57, 1846−1850.

(39) Wu, Y.; Nie, P.; Wu, L.; Dou, H.; Zhang, X. 2D MXene/SnS2 Composites as High-Performance Anodes for Sodium Ion Batteries. Chem. Eng. J. 2018, 334, 932−938.

(40) Tang, Q.; Zhou, Z.; Shen, P. Are MXenes Promising Anode Materials for Li Ion Batteries? Computational Studies on Electronic Properties and Li Storage

Capability of Ti3C2 and Ti3C2X2 (X = F, OH) Monolayer. J. Am. Chem. Soc. 2012, 134, 16909−16916.

(41) Xie, Y.; Dall'Agnese, Y.; Naguib, M.; Gogotsi, Y.; Barsoum, M. W.; Zhuang, H. L.; Kent, P. R. C. Prediction and Characterization of MXene Nanosheet Anodes for Non-Lithium-Ion Batteries. ACS Nano 2014, 8, 9606−9615.

(42) Wang, X.; Shen, X.; Gao, Y.; Wang, Z.; Yu, R.; Chen, L. Atomic-Scale Recognition of Surface Structure and Intercalation Mechanism of Ti3C2X. J. Am. Chem. Soc. 2015, 137, 2715−2721.

(43) Kajiyama, S.; Szabova, L.; Sodeyama, K.; Iinuma, H.; Morita, R.; Gotoh, K.; Tateyama, Y.; Okubo, M.; Yamada, A. Sodium-Ion Intercalation Mechanism in MXene Nanosheets. ACS Nano 2016, 10, 3334−3341.

(44) Hu, M.; Li, Z.; Zhang, H.; Hu, T.; Zhang, C.; Wu, Z.; Wang, X. Self-Assembled Ti3C2Tx MXene Film with High Gravimetric Capacitance. Chem. Commun. 2015, 51, 13531−13533.

(45) Hu, M.; Li, Z.; Hu, T.; Zhu, S.; Zhang, C.; Wang, X. HighCapacitance Mechanism for Ti3C2Tx MXene by in Situ Electrochemical Raman Spectroscopy Investigation. ACS Nano 2016, 10, 11344−11350.

(46) Wexler, A. Vapor Pressure Formulation for Water in Range 0 to 100 °C. A Revision. J. Res. Natl. Bur. Stand., Sect. A 1976, 80, 775− 785.

(47) Hu, T.; Wang, J.; Zhang, H.; Li, Z.; Hu, M.; Wang, X. Vibrational Properties of Ti3C2 and Ti3C2T2 (T = O, F, OH) Monosheets by First-Principles Calculations: a Comparative Study. Phys. Chem. Chem. Phys. 2015, 17, 9997−10003.

(48) Hu, T.; Li, Z.; Hu, M.; Wang, J.; Hu, Q.; Li, Q.; Wang, X. Chemical Origin of Termination-Functionalized MXenes: Ti3C2T2 as a Case Study. J. Phys. Chem. C 2017, 121, 19254−19261.

(49) Hu, T.; Hu, M.; Gao, B.; Li, W.; Wang, X. Screening Surface Structure of MXenes by High-Throughput Computation and Vibrational Spectroscopic Confirmation. J. Phys. Chem. C 2018, 122, 18501−18509.

(50) Asahi, R.; Morikawa, T.; Ohwaki, T.; Aoki, K.; Taga, Y. VisibleLight Photocatalysis in Nitrogen-Doped Titanium Oxides. Science 2001, 293, No. 269.

(51) Sathish, M.; Viswanathan, B.; Viswanath, R. P.; Gopinath, C. S. Synthesis, Characterization, Electronic Structure, and Photocatalytic Activity of Nitrogen-Doped TiO2 Nanocatalyst. Chem. Mater. 2005, 17, 6349−6353.

(52) Wang, J.; Tafen, D. N.; Lewis, J. P.; Hong, Z.; Manivannan, A.; Zhi, M.; Li, M.; Wu, N. Origin of Photocatalytic Activity of NitrogenDoped TiO2 Nanobelts. J. Am. Chem. Soc. 2009, 131, 12290−12297.

(53) Riley, D. P.; Kisi, E. H. The Design of Crystalline Precursors For the Synthesis of Mn−1AXn Phases and Their Application to Ti3AlC2. J. Am. Ceram. Soc. 2007, 90, 2231−2235.

(54) Middleburgh, S. C.; Lumpkin, G. R.; Riley, D. Accommodation, Accumulation, and Migration of Defects in Ti3SiC2 and Ti3AlC2 MAX Phases. J. Am. Ceram. Soc. 2013, 96, 3196−3201.

(55) Hu, T.; Yang, J.; Wang, X. Carbon Vacancies in Ti2CT2 MXenes: Defects or a New Opportunity? Phys. Chem. Chem. Phys. 2017, 19, 31773−31780.

(56) Kissinger, P. T.; Heineman, W. R. Cyclic Voltammetry. J. Chem. Educ. 1983, 60, 702−706.

(57) Wang, J.; Polleux, J.; Lim, J.; Dunn, B. Pseudocapacitive Contributions to Electrochemical Energy Storage in TiO2 (Anatase) Nanoparticles. J. Phys. Chem. C 2007, 111, 14925−14931.

(58) Xu, J.; Jia, C.; Cao, B.; Zhang, W. F. Electrochemical Properties of Anatase TiO2 Nanotubes as an Anode Material for Lithium-Ion Batteries. Electrochim. Acta 2007, 52, 8044−8047.

(59) Winter, M.; Besenhard, J. O.; Spahr, M. E.; Novak, P. Insertion´ Electrode Materials for Rechargeable Lithium Batteries. Adv. Mater. 1999, 10, 725−763.

(60) Simon, P. Two-Dimensional MXene with Controlled Interlayer Spacing for Electrochemical Energy Storage. ACS Nano 2017, 11, 2393−2396.

(61) Aurbach, D. Review of Selected Electrode−Solution Interactions Which Determine the Performance of Li and Li Ion Batteries. J. Power Sources 2000, 89, 206−218.

(62) Yu, X.; Yun, S.; Yeon, J. S.; Bhattacharya, P.; Wang, L.; Lee, S. W.; Hu, X.; Park, H. S. Emergent Pseudocapacitance of 2D Nanomaterials. Adv. Energy Mater. 2018, 8, No. 1702930.

(63) Aurbach, D.; Markovsky, B.; Weissman, I.; Levi, E.; Ein-Eli, Y. On the Correlation Between Surface Chemistry and Performance of Graphite Negative Electrodes for Li Ion Batteries. Electrochim. Acta 1999, 45, 67−86.

(64) Ohzuku, T.; Ueda, A.; Yamamoto, N. Zero-Strain Insertion Material of Li[Li1/3Ti5/3]O4 for Rechargeable Lithium Cells. J. Electrochem. Soc. 1995, 142, 1431−1435.

(65) Hu, T.; Hu, M.; Li, Z.; Zhang, H.; Zhang, C.; Wang, J.; Wang, X. Interlayer Coupling in Two-Dimensional Titanium Carbide MXenes. Phys. Chem. Chem. Phys. 2016, 18, 20256−20260.

(66) Sen, U. K.; Johari, P.; Basu, S.; Nayak, C.; Mitra, S. An Experimental and Computational Study to Understand the Lithium Storage Mechanism in Molybdenum Disulfide. Nanoscale 2014, 6, 10243−10254.

(67) Brezesinski, T.; Wang, J.; Tolbert, S. H.; Dunn, B. Ordered Mesoporous α-MoO3 with Iso-Oriented Nanocrystalline Walls for Thin-Film Pseudocapacitors. Nat. Mater. 2010, 9, No. 146.

(68) Chao, D.; Zhu, C.; Yang, P.; Xia, X.; Liu, J.; Wang, J.; Fan, X.; Savilov, S. V.; Lin, J.; Fan, H. J.; et al. Array of Nanosheets Render Ultrafast and High-Capacity Na-Ion Storage by Tunable Pseudocapacitance. Nat. Commun. 2016, 7, No. 12122.

(69) Huang, S.; Zhang, L.; Lu, X.; Liu, L.; Liu, L.; Sun, X.; Yin, Y.; Oswald, S.; Zou, Z.; Ding, F.; et al. Tunable Pseudocapacitance in 3D TiO2−δ Nanomembranes Enabling Superior Lithium Storage Performance. ACS Nano 2017, 11, 821−830.

(70) Augustyn, V.; Come, J.; Lowe, M. A.; Kim, J. W.; Taberna, P.- L.; Tolbert, S. H.; Abruña, H. D.; Simon, P.; Dunn, B. High-Rate Electrochemical Energy Storage Through Li+ Intercalation Pseudocapacitance. Nat. Mater. 2013, 12, No. 518.

(71) Augustyn, V.; Simon, P.; Dunn, B. Pseudocapacitive Oxide Materials for High-Rate Electrochemical Energy Storage. Energy Environ. Sci. 2014, 7, 1597−1614.

(72) Cui, C.; Hu, M.; Zhang, C.; Cheng, R.; Yang, J.; Wang, X. High-Capacitance Ti3C2Tx MXene Obtained by Etching Submicron Ti3AlC2 Grains Grown in Molten Salt. Chem. Commun. 2018, 54, 8132−8135.